Design and dynamic modeling of electrorheological fluid-based variable-stiffness fin for robotic fish

2017 Smart Mater. Struct. 26 085014

(http://iopscience.iop.org/0964-1726/26/8/085014)

IOP Publishing Smart Materials and Structures

Smart Mater. Struct. **26** (2017) 085014 (15pp) https://doi.org/10.1088/1361-665X/aa7238

Design and dynamic modeling of electrorheological fluid-based variable-stiffness fin for robotic fish

Sanaz Bazaz Behbahani and Xiaobo Tan[1]

Smart Microsystems Laboratory, Department of Electrical and Computer Engineering, Michigan State University, East Lansing, MI 48824, United States of America

E-mail: bazazbeh@msu.edu and xbtan@msu.edu

Received 4 January 2017, revised 22 April 2017
Accepted for publication 10 May 2017
Published 10 July 2017

Abstract

Fish actively control their stiffness in different swimming conditions. Inspired by such an adaptive behavior, in this paper we study the design, prototyping, and dynamic modeling of compact, tunable-stiffness fins for robotic fish, where electrorheological (ER) fluid serves as the enabling element. A multi-layer composite fin with an ER fluid core is prototyped and utilized to investigate the influence of electrical field on its performance. Hamilton's principle is used to derive the dynamic equations of motion of the flexible fin, and Lighthill's large-amplitude elongated-body theory is adopted to estimate the hydrodynamic force when the fin undergoes base-actuated rotation. The dynamic equations are then discretized using the finite element method, to obtain an approximate numerical solution. Experiments are conducted on the prototyped flexible ER fluid-filled beam for parameter identification and validation of the proposed model, and for examining the effectiveness of electrically controlled stiffness tuning. In particular, it is found that the natural frequency is increased by almost 40% when the applied electric field changes from 0 to 1.5×10^6 V m^{-1}.

Keywords: electrorheological fluid, dynamic model, stiffness tuning, Lighthill's theory, Hamilton's principle, finite element method (FEM), robotic fish

(Some figures may appear in colour only in the online journal)

1. Introduction

Fish propel in water by moving different fins or deforming the body [1, 2], which has inspired the development of robotic fish that accomplish locomotion in ways that emulate those of biological fish [3–8]. Compared with rigid fins, flexible fins and fin joints introduce additional dynamic behavior that can be exploited to enhance robotic fish performance [9–19]. The optimal flexibility, however, typically changes with factors such as fin-beat frequency or amplitude [7, 8, 20, 21]. For example, with an increased fin-beat frequency and amplitude, the optimal stiffness tends to increase [17, 22, 23]. The connection between propulsor stiffness and swimming performance has also been studied for biological fish, which sheds interesting insight into the design of flexible propulsors for robotic fish [24–26].

The discussions above indicate that it is of interest to actively tune the fin stiffness for robotic fish according to swimming conditions, and there has been some limited work reported in this area over the past few years [27–29]. Ziegler *et al* [27] introduced a tail-actuated robotic fish, where the tail fin was capable of changing its elasticity, which was realized by actively inserting additional foils into the tail fin or removing these foils from the fin using two servo motors. Park *et al* [28] designed a fin with a variable-stiffness flapping mechanism, which was realized by compressing a compliant material to increase the stiffness. The designed tail consisted of six rigid plates, also used as the backbone of the fish. Two tendons were used for driving the tail and two other tendons were used to change its stiffness. In particular, when the latter tendons were pulled, the variable stiffness structure would be

[1] Author to whom any correspondence should be addressed.

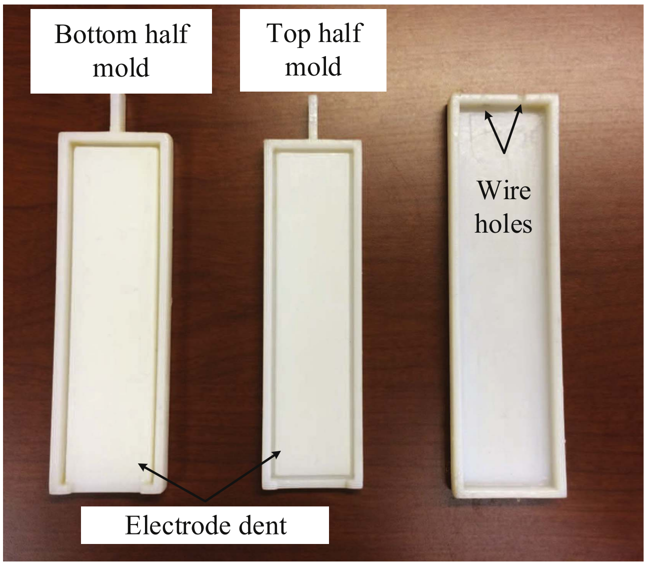

Figure 1. 3D-printed molds used to prototype the variable stiffness fin.

compressed and result in an increase in axial stiffness. Nakabayashi *et al* [29] developed a robotic fish with a variable stiffness mechanism using a variable effective-length spring mechanism, achieved by altering the length of a rigid plate, which resulted in changing the effective-length of the spring and hence the stiffness. All these reported mechanisms involved multiple discrete parts and were bulky and complex.

In this work, we propose a compact mechanism for fin stiffness tuning using electrorheological (ER) fluid. The ER fluid typically consists of a base liquid (usually silicone oil) with suspended polymer particles. An ER fluid experiences changes in rheological properties in the presence of an electric field, going from the liquid phase to a solid gel phase as the electric field increases. In particular, the particles tend to align with the electric field line, resulting in changes in viscosity, yield stress, and some other properties of the fluid. The response time of the ER fluid is in the order of milliseconds, which provides a fast solution for stiffness tuning. ER fluids have a range of engineering applications, such as shock absorbers [30], brakes and clutch systems [31], and vibration control [32–34].

The proposed stiffness-tuning fin consists of an ER fluid-filled urethane rubber, with embedded copper sheets as electrodes. Following the framework presented in [34], a dynamic model for the fin is developed using the Hamilton's principle. One key difference between this work and [34], however, is that the latter was concerned with vibration control in air while this work deals with soft fins actuated in water. Consequently, we need to capture the hydrodynamic forces on the fin, which are modeled with (slightly adapted) large-amplitude elongated body theory proposed by Lighthill [35]. The final equations of motion are obtained through a finite-element procedure and solved numerically. Experiments are conducted on a fin prototype to examine the performance of stiffness-tuning, identify model parameters (including, in particular, the complex shear modulus of the ER fluid under different electric fields, and the hydrodynamic function), and validate the proposed dynamic model. First, for a given electric field, passive damped vibration of the flexible fin in air is measured to extract the natural frequency and damping ratio, which are used subsequently to identify the complex shear modulus of the ER fluid. Next, a similar procedure is repeated in water to identify the complex hydrodynamic coefficient of the flexible fin. Finally, the behavior of the base-actuated oscillation is studied, in an anchored robotic fish body setup, to validate the proposed dynamic model. Specifically, good match between the measured beam shape and tip deflection and their model predictions indicate the efficacy of the model. The experiments also demonstrate the fin's capability in modulating stiffness. For example, when the electric field is increased from 0 to 1.5×10^6 V m^{-1}, the fin's natural frequency increases from 8.1 to 10.1 Hz in air (25% change), and from 3.6 to 5.1 Hz in water (40% change).

A preliminary version of this work was presented at the 2015 ASME Dynamic Systems and Control Conference [36]. The improvements of this paper over [36] include the following. First, on the modeling side, the framework for the hydrodynamic force calculation is revised. We now use a complex hydrodynamic coefficient to capture the beam-fluid interactions more accurately. In addition, the actual ER fluid-filled flexible fin proposed in this paper consists of 5 layers (compared to the 3 layers fin presented in [36]) and the equations of motion are updated accordingly. Calculation of the external force is also presented in this paper for the first time. Second, on the simulation side, data reported here were generated using the updated equations and parameters. Third, while the previous work [36] focused only on modeling and simulation, this manuscript presents results on flexible fin prototyping and experimental model validation. All figures involving data in this paper are different from those in [36]. Finally, the writing has been polished throughout the paper.

The organization of the remainder of this paper is as follows. First, the fabrication procedure of the ER fluid-filled fin is presented in section 2. In section 3, the dynamic model is described. The experimental results are provided in section 4, where the effect of changing the electric field on the fin stiffness is studied and the proposed dynamic model is validated. Finally, concluding remarks are provided in section 5.

2. Fabrication procedure

2.1. Materials

The ER fluid used in this study is LID-3354D from Smart Technology Ltd., West Midlands, England. This fluid consists of 37.5% of sub-45 μm polymer particles in a density-matched silicone oil. The density of the ER fluid is 1460 Kg m^{-3}

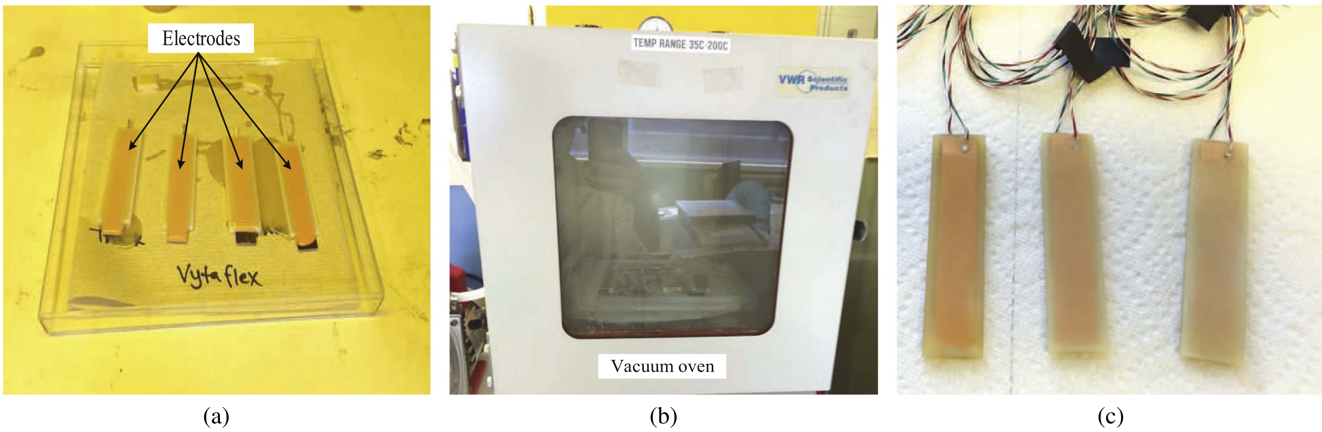

Figure 2. Prototyping the variable-stiffness fin: (a) the halves of the fin, with electrodes incorporated; (b) degassing the parts in a vacuum oven; (c) final product: hollow fins with wires attached to the electrodes.

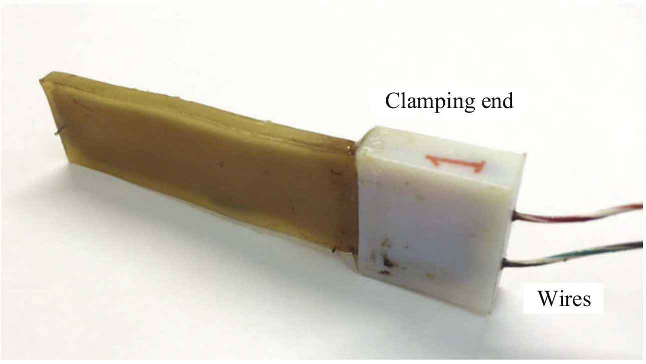

Figure 3. Prototyped variable-stiffness fin with ER fluid filled.

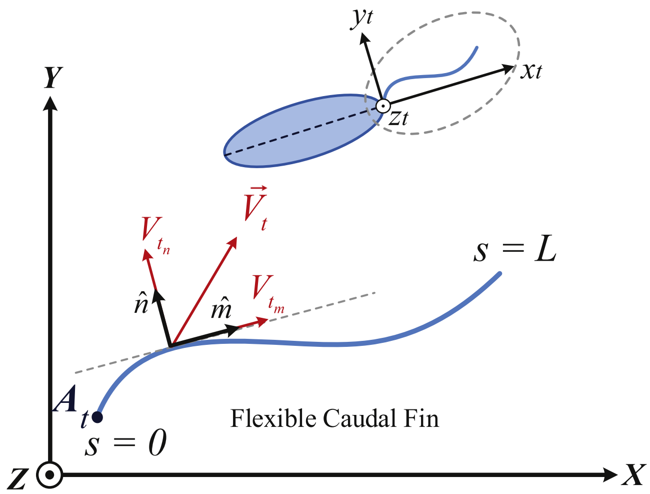

Figure 4. Planar view of the robotic fish and the detailed illustration of the flexible tail coordinate system.

and the viscosity is 110 mPa s at 30 °C. Two thin copper foils (Copper 110, 99.9% pure, from Basic Copper, Carbondale, IL, USA) with dimensions of 15 mm × 8 mm × 0.035 mm are used as the electrodes. The flexible encasing is made of Vytaflex10, which is a liquid urethane rubber from Smooth-On Inc., Macungie, PA, USA. This rubber has a density of 1000 Kg m^{-3}.

2.2. Manufacturing procedure

The prototyping of the variable-stiffness fin is done in multiple stages. First, three different molds are designed and 3D-printed for the encasing: Bottom half, top half, and that for assembling the two halves. The actual 3D-printed molds are shown in figure 1. The molds are designed to make a fin with dimensions of 65 mm × 20 mm × 4 mm, which are representative of robotic fish fin sizes reported in the literature [12]. The bottom and top molds have a small dent in them to secure the electrodes in place. A gap of 1.5 mm is formed between the two electrodes, where the ER fluid will be injected. In the first step, the copper electrodes are cut and placed in the designed dent in each mold, and the Vytaflex mixture is poured over them. The parts are placed in a vacuum chamber for degassing (38.7 mbar of vacuum for 5 min), and is set to cure for 24 h. Next, we remove the two prototyped halves of the fin from the molds, attach a wire to each electrode, put both in the third mold, pour Vytaflex mixture, degas, and let it cure for another 24 h. The resulting prototype is a hollow, flexible fin with the electrodes and wires incorporated. The described prototyping steps are illustrated in figure 2. Finally, a 3D-printed rigid clamping part is attached to the wire end of the fin and the ER fluid is injected from the posterior end of the beam into the hollow gap between the two halves and the injection holes are sealed afterward. Figure 3 shows a final ER fluid-filled prototype.

3. Dynamic model for the variable-stiffness fin

Although the presented fabrication procedure in section 2 can be used to make different variable-stiffness fins (such as caudal fin, pectoral fin, among others), this study is focused

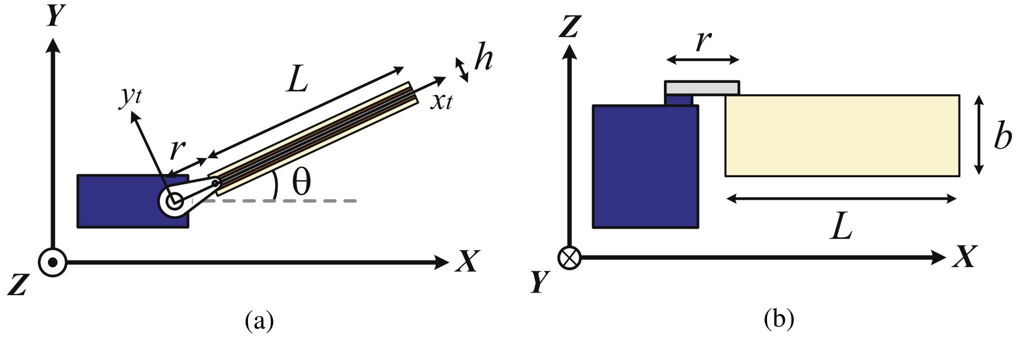

Figure 5. Schematic for actuation of the ER fluid-filled caudal fin. (a) Top view, (b) side view.

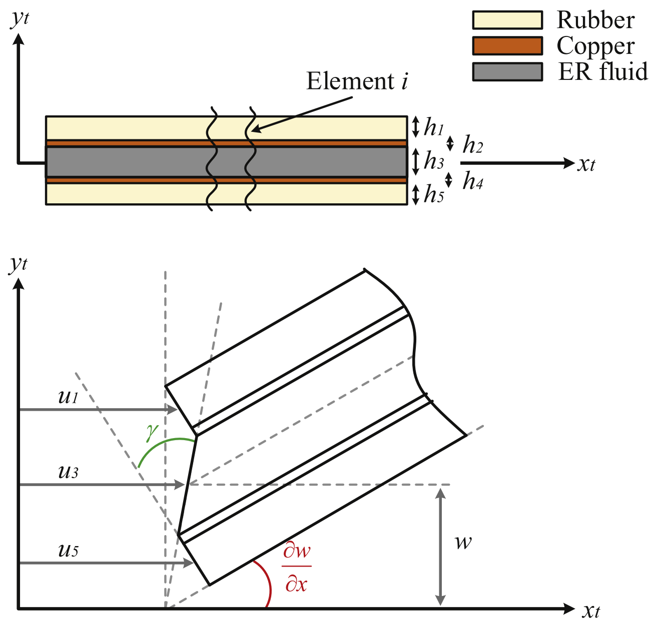

Figure 6. Schematics of the deflected ER fluid-filled flexible fin (adapted from figure 3 [34], copyright © 2007 by SAGE Publications. Reprinted by Permission of SAGE Publications, Ltd.).

on the use for the caudal fin (tail). To simplify the modeling procedure, we consider the robotic fish body to be anchored, so the calculations of the body dynamics are not covered in this paper. The motion of the variable-stiffness caudal fin, filled with ER fluid, is modeled using Hamilton's principle. The resulting equations of motion are complex and highly nonlinear, so finite element method (FEM) is used to numerically solve the equations.

3.1. Evaluation of hydrodynamic force using Lighthill's large-amplitude elongated-body theory

The hydrodynamic force on the variable-stiffness fin is evaluated using Lighthill's large-amplitude elongated-body theory, which was developed to study the carangiform swimming mode of a fish [35]. As illustrated in figure 4, $[X, Y, Z]^T$ is the inertial frame, $[x_t, y_t, z_t]^T$ are the tail-fixed coordinate (origin at the base of the tail), and $(\hat{m}, \hat{n})$ are the unit vectors tangential and perpendicular to the flexible fin, respectively. The robotic fish is assumed to have a planar motion in the XY-plane. We assume that the water far from the robotic fish body is at rest, and the extensibility of the caudal fin is negligible. The Lagrangian coordinate s indicates a point on the flexible tail and its distance from the base of the fin, which varies from 0 to L (length of the caudal fin). The location of each point on the fin at time t, in the inertial frame, is denoted as $(x(s, t), y(s, t))$. The inextensibility assumption is expressed as

$$\left(\frac{\partial x}{\partial s}\right)^2 + \left(\frac{\partial y}{\partial s}\right)^2 = 1. \tag{1}$$

The tangential $(\hat{m})$ and normal $(\hat{n})$ unit vectors are represented as

$$\hat{m} = \left(\frac{\partial x}{\partial s}, \frac{\partial y}{\partial s}\right), \tag{2}$$

$$\hat{n} = \left(-\frac{\partial y}{\partial s}, \frac{\partial x}{\partial s}\right). \tag{3}$$

The velocity vector of the caudal fin $\vec{V}_t = (\partial x/\partial t, \partial y/\partial t)$ has tangential and normal components, represented respectively by,

$$V_{t_m} = \langle \vec{V}_t, \hat{m} \rangle = \frac{\partial x}{\partial t}\frac{\partial x}{\partial s} + \frac{\partial y}{\partial t}\frac{\partial y}{\partial s}, \tag{4}$$

$$V_{t_n} = \langle \vec{V}_t, \hat{n} \rangle = \frac{\partial y}{\partial t}\frac{\partial x}{\partial s} - \frac{\partial x}{\partial t}\frac{\partial y}{\partial s}, \tag{5}$$

where $\langle \cdot, \cdot \rangle$ denotes the inner product of the vectors. Finally, the hydrodynamic force density experienced by the caudal fin, due to the added-mass effect, for $s < L$, is obtained as

$$\vec{f}_h(s) = -m_v \Gamma \frac{\mathrm{d}}{\mathrm{d}t} V_{t_n} \hat{n}, \tag{6}$$

where m_v denotes the virtual mass of the tail and is approximated by $\frac{1}{4}\pi\rho b^2$, with ρ indicating the density of water and b denoting the depth of the caudal fin in the z_t direction. Note that equation (6) is slightly adapted from the

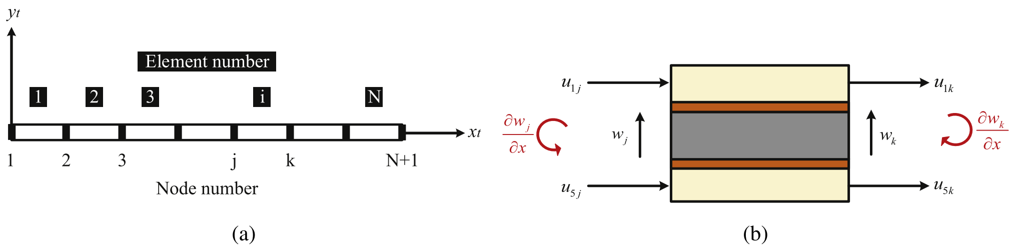

Figure 7. Schematic of the flexible fin in FEM: (a) configuration of the element and node numbers, (b) element *i*, its two nodes, and degrees of freedom.

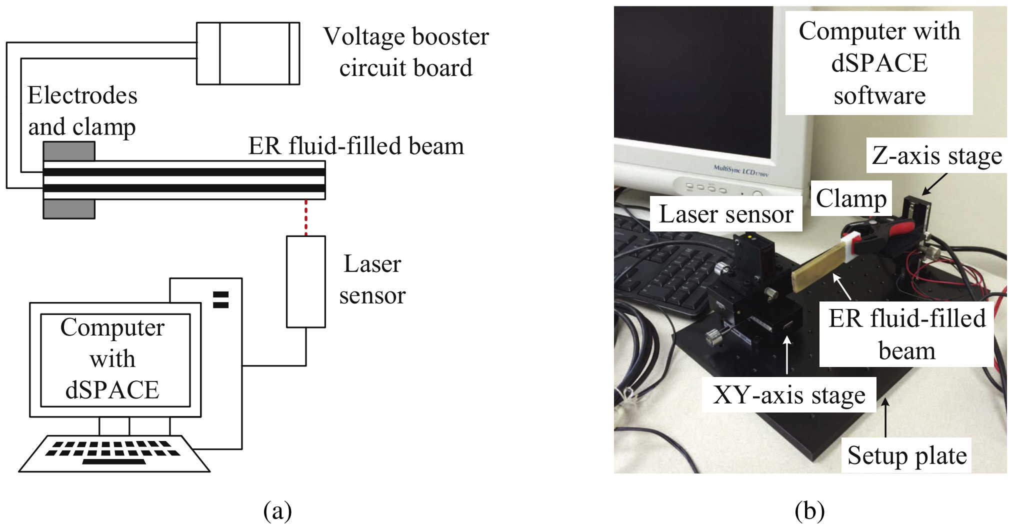

Figure 8. Experimental setup for observing passive, damped vibration of the ER fluid-filled flexible fin under different electric fields. (a) Schematic, (b) actual.

original Lighthill model, which does not include the term Γ that represents the complex hydrodynamic coefficient. Including the hydrodynamic coefficient enables more accurate capturing of the beam-fluid interactions [37, 38]. At $s = L$, there is a concentrated force calculated as

$$\vec{F}_{h_L} = \left[m_v V_{t_n} V_{t_m} \hat{n} - \frac{1}{2} m_v V_{t_n}^2 \hat{m} \right]_{s=L}. \tag{7}$$

3.2. Dynamic modeling of the variable-stiffness caudal fin filled with ER fluid

We need the information about the movement of the flexible tail, particularly its normal and tangential velocity components at each point, to determine the hydrodynamic forces and moments on the fin. For this purpose, we follow [34, 39–41] and use Hamilton's principle to develop the equations of motion of the flexible tail.

The variable-stiffness fin has a five-layer structure. It consists of an ER fluid core with two copper foil layers around it, which is further encased by the flexible rubber on both sides. Driven by a servomotor, the fin can oscillate at its base with the oscillation angle given by

$$\theta(t) = \theta_A \sin(\omega_\theta t), \tag{8}$$

where θ_A is the amplitude (in degree) and ω_θ is the angular frequency of the fin actuation. Figure 5 shows the actuation schematic for the fin, which has a length of L, thickness of h, and depth of b.

3.2.1. ER fluid. An ER fluid is a type of smart fluid that changes rheological properties in the presence of an electric field. Typically an ER fluid consists of a non-polar liquid with dielectric particles suspended in it. The fluid changes state from liquid (in the absence of an electric field) to a solid gel form (in the presence of a strong electric field), when the suspended particles are aligned with the lines of the electric field [42, 43].

When filled in a multi-layer beam configuration, the fluid functions in its pre-yield (static) regime and behaves as a viscoelastic material [44, 45]. Therefore, its property can be modeled with a parameter called complex shear modulus (G^*). The linear relationship between shear stress, τ, and

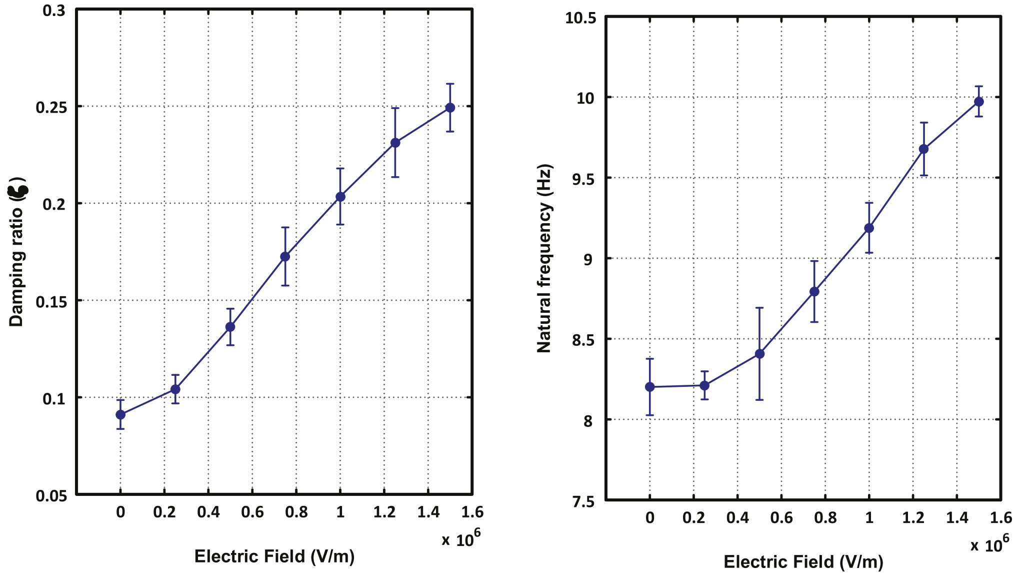

(a) (b)

Figure 9. Identified parameters under different electric fields in the air. (a) Damping ratio, (b) natural frequency.

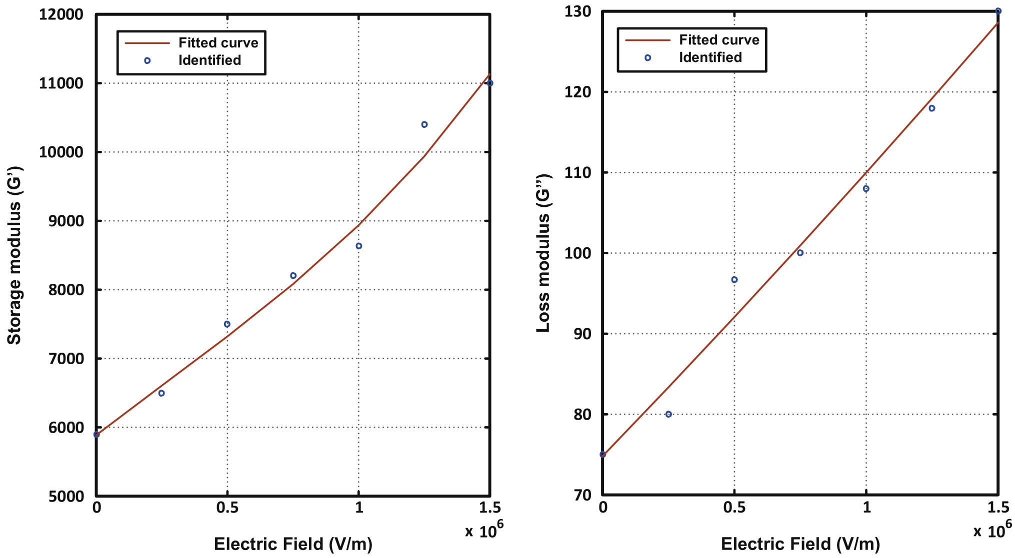

(a) (b)

Figure 10. Identified complex shear modulus values and the fitted curve under different electric fields. (a) Storage modulus (G'), (b) loss modulus (G'').

shear strain, γ, is as follows:

$$\tau = G^* \gamma, \tag{9}$$

where G^* is a function of the electric field and consists of a storage modulus (G') and a loss modulus (G'') [34]:

$$G^* = G' + \mathrm{i}G''. \tag{10}$$

3.2.2. Multi-layer Beam. To model the flexible fin filled with ER fluid, first, some kinematic relationships need to be defined. We make a few assumptions to simplify these kinematic relationships: There is no slippage between the ER fluid layer and the electrodes; the transverse displacement (along the y_r-axis) is the same for all the layers; there is no normal stress in the ER fluid layer and there is no shear strain in the electrodes or in the rubber layers; the rubber and copper layers are bonded perfectly, resulting in the same displacement in longitudinal direction. Therefore, the shear strain, γ, and the longitudinal deflection of the ER fluid layer, u_3, is expressed as

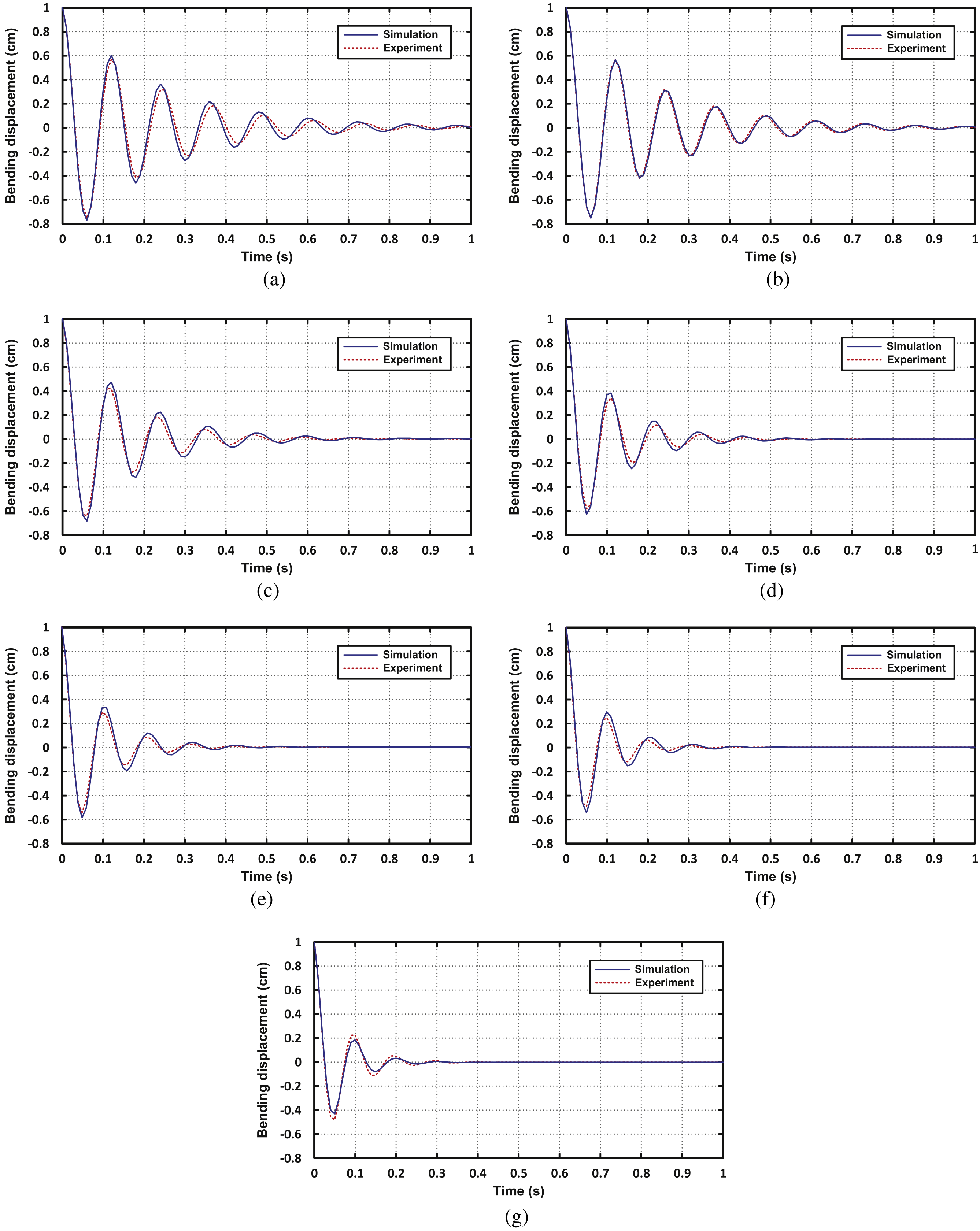

Figure 11. A sample of experimentally measured damped oscillations of the beam tip in air, along with simulation results corresponding to the matched parameters, for each applied electric field. (a) $E_f = 0$, (b) $E_f = 0.25 \times 10^6$, (c) $E_f = 0.5 \times 10^6$, (d) $E_f = 0.75 \times 10^6$, (e) $E_f = 1 \times 10^6$, (f) $E_f = 1.25 \times 10^6$, (g) $E_f = 1.5 \times 10^6$ V m^{-1}.

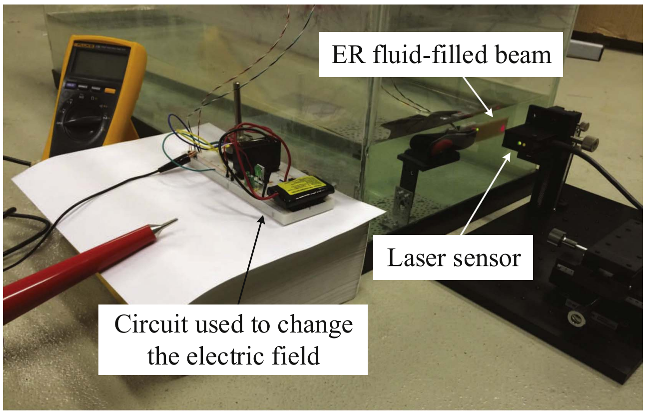

Figure 12. Experimental setup for measuring damped oscillations of the flexible fin in water.

follows [40, 41]

$$\gamma = \frac{u_1 - u_5}{h_3} + \frac{h}{h_3}\frac{\partial w}{\partial x}, \tag{11}$$

$$u_3 = \frac{u_1 + u_5}{2} + \frac{(h_1 + h_2) - (h_4 + h_5)}{4}\frac{\partial w}{\partial x}, \tag{12}$$

where u_k ($k = 1,\ldots,5$) are the longitudinal displacements of the mid-plane of the kth layer with ($u_1 = u_2$) and ($u_4 = u_5$), w is the transverse displacement of the beam, h_k ($k = 1,\ldots,5$) is the thickness of the kth layer, with $h = h_1/2 + h_2 + h_3 + h_4 + h_5/2$, and $\frac{\partial w}{\partial x}$ is the deflection angle. A schematic of a portion of the ER fluid-filled flexible fin, in a deflected configuration, is shown in figure 6.

The governing equations of motion for the variable stiffness flexible fin filled with ER fluid are obtained using the Hamilton's principle, which is described as follows

$$\int_{t_1}^{t_2} \delta(T - U + W)\mathrm{d}t = 0, \tag{13}$$

where T is the kinetic energy, U is the potential energy, W is the work done by external loads, and δ is the variational operator throughout the flexible caudal fin. The kinetic energy is determined as

$$T = \frac{1}{2}\int_0^L \sum_{k=1}^{5} \rho_k A_k \dot{r}_k^T \dot{r}_k \, dx + \frac{1}{2}J\dot{\theta}^2, \tag{14}$$

where ρ_k is the density of the kth layer, A_k is the cross-sectional area of the kth layer ($A_k = b_k h_k$), where $k = 1,\ldots,5$, L denotes the length of the fin, and J is the moment of inertia associated with the servomotor actuation. The velocity vector $\dot{r}_k$ is defined as

$$\dot{r}_k = (\dot{u}_k - w\dot{\theta})\hat{x}_t + (x\dot{\theta} + u_k\dot{\theta} + \dot{w})\hat{y}_t, \tag{15}$$

where $\hat{x}_t$ and $\hat{y}_t$ are the unit vectors in the x_t and y_t directions, respectively.

The potential energy is calculated as follows

$$U = \frac{1}{2}\int_0^L \Bigg[\sum_{k=1,2,4,5}\left(E_k A_k\left(\frac{\partial u_k}{\partial x}\right)^2 + E_k I_k\left(\frac{\partial^2 w}{\partial x^2}\right)^2\right) + G^* A_3 \gamma^2 + mb\dot{\theta}^2\left[\frac{1}{2}(L^2 - x^2) + r(L - x)\right]\left(\frac{\partial w}{\partial x}\right)^2\Bigg]\mathrm{d}x, \tag{16}$$

where E_k is the Young's modulus of the kth layer, I_k is the moment of inertia of the kth layer, m is the total mass of the fin, x is the distance from fixed end of the fin, and r is the servo arm length.

The total work done by the external forces (servo arm and hydrodynamic forces) are defined as follows

$$W = \tau\theta + \int_0^L (f_{h_x} u_3 + f_{h_y} w)\,\mathrm{d}x + F_{h_{Lx}} u_3 + F_{h_{Ly}} w, \tag{17}$$

where τ is the rotational torque from the servomotor, the hydrodynamic force densities f_{h_x} and f_{h_y} represent the x-component and y-component of $\vec{f}_h$ defined in equation (6), respectively, and the hydrodynamic forces $F_{h_{Lx}}$ and $F_{h_{Ly}}$ represent the x-component and y-component of $\vec{F}_{h_L}$ defined in equation (7), respectively.

By substituting equations (14), (16), and (17) into equation (13), we obtain the dynamic equations of motion:

$$\begin{aligned}
&\left(\rho_1 A_1 + \rho_2 A_2 + \frac{1}{4}\rho_3 A_3\right)\ddot{u}_1 + \frac{1}{4}\rho_3 A_3 \ddot{u}_5 \\
&-2\left(\rho_1 A_1 + \rho_2 A_2 + \frac{1}{2}\rho_3 A_3\right)w\ddot{\theta} \\
&-3\left(\rho_1 A_1 + \rho_2 A_2 + \frac{1}{2}\rho_3 A_3\right)\dot{w}\dot{\theta} \\
&-(\rho_1 A_1 + \rho_2 A_2)(r + x + u_1)\dot{\theta}^2 \\
&-\frac{1}{2}\rho_3 A_3\left(r + x + \frac{u_1 + u_5}{2}\right)\dot{\theta}^2 \\
&+\frac{1}{2}(E_1 A_1 + E_2 A_2)\frac{\partial}{\partial u_1}\left(\frac{\partial u_1}{\partial x}\right)^2 \\
&+\frac{G^* A_3}{h_3^2}(u_1 - u_5) = 0,
\end{aligned} \tag{18}$$

$$\begin{aligned}
&\left(\frac{1}{4}\rho_3 A_3 + \rho_4 A_4 + \rho_5 A_5\right)\ddot{u}_5 + \frac{1}{4}\rho_3 A_3 \ddot{u}_1 \\
&-2\left(\frac{1}{2}\rho_3 A_3 + \rho_4 A_4 + \rho_5 A_5\right)w\ddot{\theta} \\
&-3\left(\frac{1}{2}\rho_3 A_3 + \rho_4 A_4 + \rho_5 A_5\right)\dot{w}\dot{\theta} \\
&-(\rho_4 A_4 + \rho_5 A_5)(r + x + u_5)\dot{\theta}^2 \\
&-\frac{1}{2}\rho_3 A_3 (r + x + \frac{u_1 + u_5}{2})\dot{\theta}^2 \\
&+\frac{1}{2}(E_4 A_4 + E_5 A_5)\frac{\partial}{\partial u_5}\left(\frac{\partial u_5}{\partial x}\right)^2 \\
&-\frac{G^* A_3}{h_3^2}(u_1 - u_5) = 0,
\end{aligned} \tag{19}$$

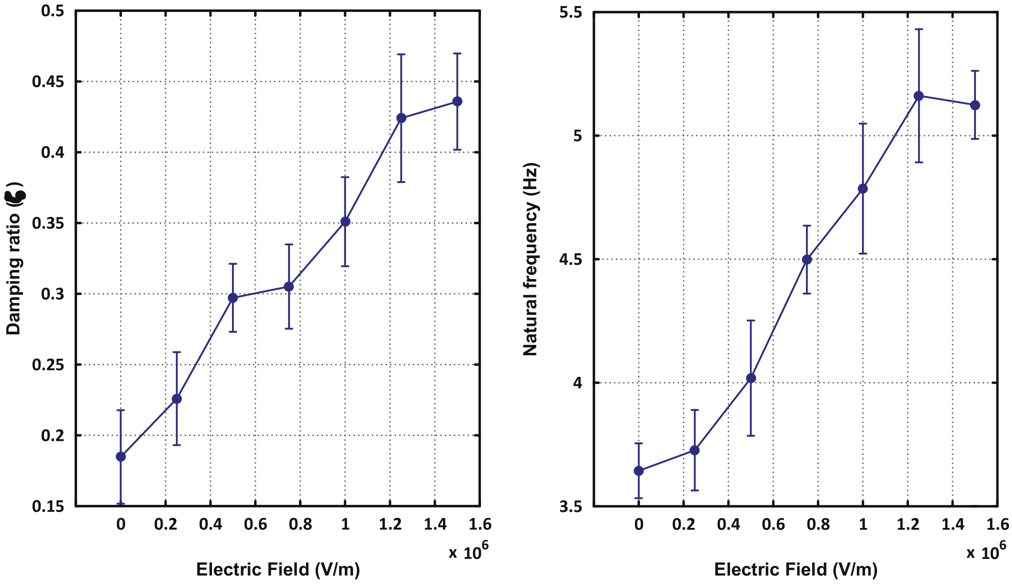

(a) (b)

Figure 13. Identified parameters under different electric fields in water. (a) Damping ratio, (b) natural frequency.

$$
\begin{aligned}
&(\rho_1 A_1 + \rho_2 A_2 + \rho_3 A_3 + \rho_4 A_4 + \rho_5 A_5)\ddot{w} \\
&\quad + (\rho_1 A_1 + \rho_2 A_2)(x + r + u_1)\ddot{\theta} \\
&\quad + (\rho_4 A_4 + \rho_5 A_5)(x + r + u_5)\ddot{\theta} \\
&\quad + \rho_3 A_3\left(x + r + \frac{u_1 + u_5}{2}\right)\ddot{\theta} \\
&\quad + 3(\rho_1 A_1 + \rho_2 A_2)\dot{u}_1\dot{\theta} + 3(\rho_4 A_4 + \rho_5 A_5)\dot{u}_5\dot{\theta} \\
&\quad + \rho_3 A_3\left(\frac{\dot{u}_1 + \dot{u}_5}{2}\right)\dot{\theta} \\
&\quad - (\rho_1 A_1 + \rho_2 A_2 + \rho_3 A_3 + \rho_4 A_4 + \rho_5 A_5) w\dot{\theta}^2 \\
&\quad + \frac{1}{2}(E_1 I_1 + E_2 I_2 + E_4 I_4 + E_5 I_5)\frac{\partial}{\partial w}\left(\frac{\partial^2 w}{\partial x^2}\right)^2 \\
&\quad + \frac{1}{2} m b \dot{\theta}^2\left[\frac{1}{2}(L^2 - x^2) + r(L - x)\right]\frac{\partial}{\partial w}\left(\frac{\partial w}{\partial x}\right)^2 \\
&\quad + G^* A_3 \frac{h^2}{h_3^2}\frac{\partial}{\partial w}\left(\frac{\partial w}{\partial x}\right)^2 - f_h w \\
&\quad + (F_{h_L - x} u_3 + F_{h_L - y} w)|_{x=L} = 0.
\end{aligned} \tag{20}
$$

3.2.3. Discretization using FEM. The equations of motion (equations (18)–(20)), which are coupled and nonlinear, are solved using FEM [39–41]. Each element consists of two nodes, and each node has four degrees of freedom. Node displacements of element i are formed by the following vector which is bounded between nodes j and k (with $k = j + 1$):

$$
\mathbf{q}_i = \left[u_{1j} \quad u_{5j} \quad w_j \quad \frac{\partial w_j}{\partial x} \quad u_{1k} \quad u_{5k} \quad w_k \quad \frac{\partial w_k}{\partial x}\right]^T. \tag{21}
$$

A schematic of the flexible fin elements and nodes, and the details of one element are shown in figure 7.

The deflection vector, represented in terms of the node deflection vector, is given by

$$
\left[u_1 \quad u_3 \quad u_5 \quad w \quad \frac{\partial w}{\partial x} \quad \gamma\right]^T = [N_1 \quad N_2 \quad N_3 \quad N_4 \quad N_5 \quad N_6]^T \mathbf{q}_i, \tag{22}
$$

where FEM shape functions N_1, N_2, N_3, N_4, N_5 and N_6 are defined as

$$
N_1 = [1 - \xi \quad 0 \quad 0 \quad 0 \quad \xi \quad 0 \quad 0 \quad 0], \tag{23}
$$

$$
N_2 = \frac{1}{2}(N_1 + N_3), \tag{24}
$$

$$
N_3 = [0 \quad 1 - \xi \quad 0 \quad 0 \quad 0 \quad \xi \quad 0 \quad 0], \tag{25}
$$

$$
N_4 = [0 \quad 0 \quad 1 - 3\xi^2 + 2\xi^3 \quad (\xi - 2\xi^2 + \xi^3)L_i \tag{26}
$$

$$
0 \quad 0 \quad 3\xi^2 - 2\xi^3 \quad (-\xi^2 + \xi^3)L_i], \tag{27}
$$

$$
N_5 = \left[\frac{\partial N_4}{\partial x}\right], \tag{28}
$$

$$
N_6 = \left[\frac{N_1 - N_3}{h_3} + \frac{h}{h_3} N_5\right], \tag{29}
$$

where $\xi = \frac{x}{L_i}$, with L_i being the length of each element.

Applying the FEM presented in equation (22) to the Hamilton's principle, we obtain the dynamic equation of

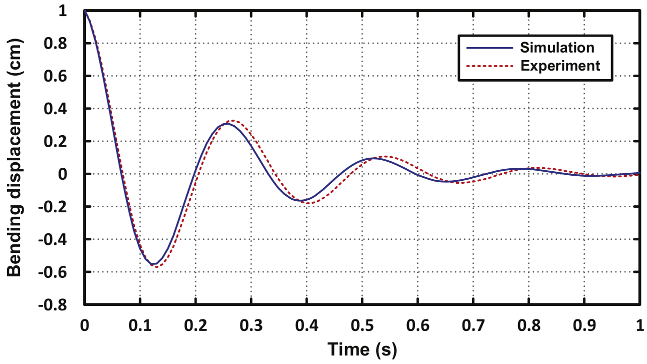

(a)

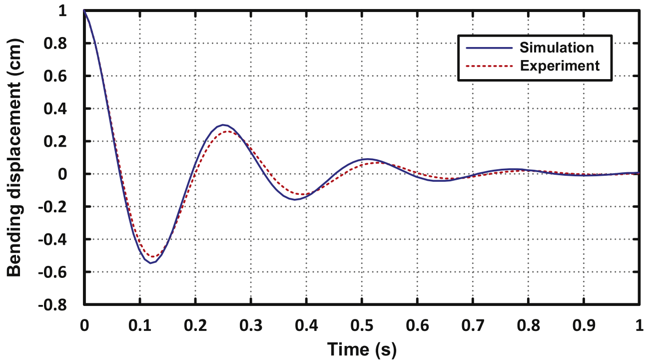

(b)

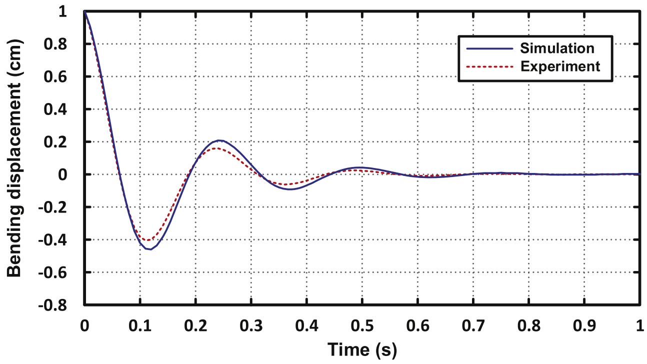

(c)

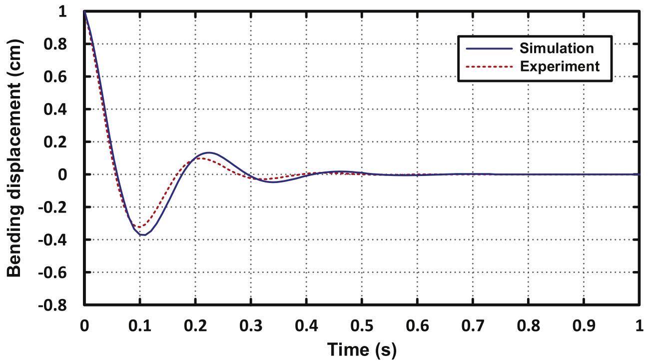

(d)

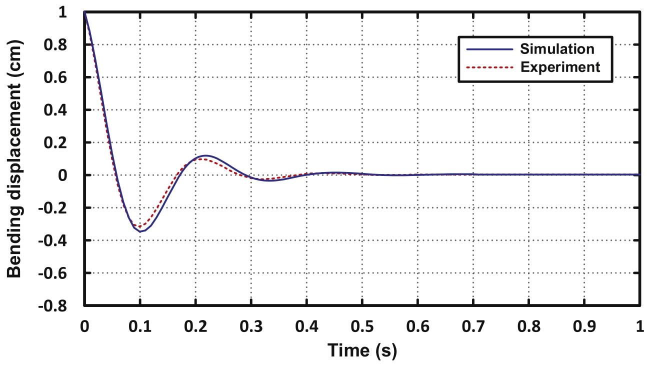

(e)

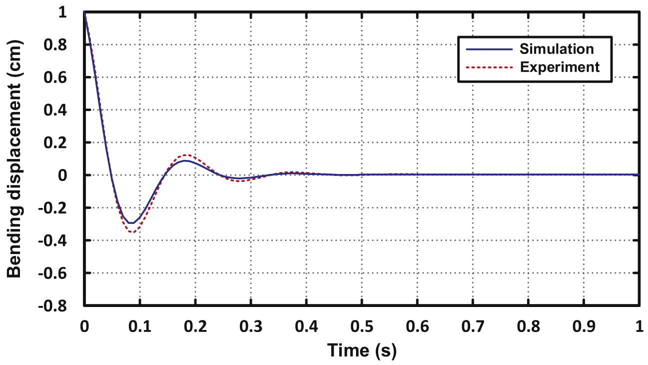

(f)

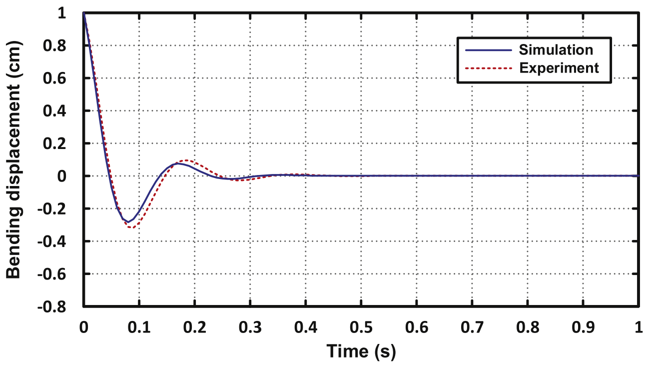

(g)

Figure 14. Passive, damped vibration of the ER fluid filled flexible beam in water: (a) $E_f = 0$, (b) $E_f = 0.25 \times 10^6$, (c) $E_f = 0.5 \times 10^6$, (d) $E_f = 0.75 \times 10^6$, (e) $E_f = 1 \times 10^6$, (f) $E_f = 1.25 \times 10^6$, (g) $E_f = 1.5 \times 10^6$ V m^{-1}.

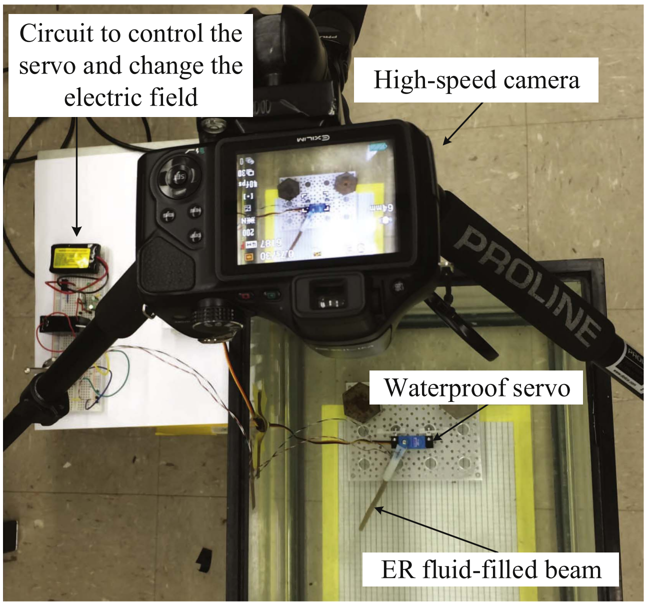

Figure 15. Experimental setup for measuring the fin shape under base actuation (top view).

motion at the elemental level:

$$\mathbf{M}_i\ddot{\mathbf{q}}_i + 2\dot{\theta}\mathbf{C}_i\dot{\mathbf{q}}_i + \mathbf{K}_i\mathbf{q}_i = \mathbf{F}_i, \tag{30}$$

where $\mathbf{M}_i$ is the element mass matrix, $\mathbf{C}_i$ is the element gyroscopic effect matrix, $\mathbf{K}_i$ is the element stiffness matrix, and $\mathbf{F}_i$ is the element force matrix, which are formed as follows:

$$\mathbf{M}_i = \int_0^{L_i}\sum_{k=1}^{5}[\rho_k A_k(N_k^T N_k + N_4^T N_4)]\ \ \mathrm{d}x, \tag{31}$$

$$\mathbf{C}_i = \int_0^{L_i}\sum_{k=1}^{5}[\rho_k A_k(N_k^T N_4 - N_k N_4^T)]\ \ \mathrm{d}x + \int_0^{L_i} G'' A_3 N_6^T N_6\ \ \mathrm{d}x, \tag{32}$$

$$\mathbf{K}_i = \mathbf{K}_{i-1} + \dot{\theta}^2(\mathbf{K}_{i-2} - \mathbf{M}_i) - \ddot{\theta}\mathbf{C}_i, \tag{33}$$

where

$$\mathbf{K}_{i-1} = \int_0^{L_i}\sum_{k=1,2,4,5}[(E_k A_k N_{k,x}^T N_{k,x} + E_k I_k N_{4,xx}^T N_{4,xx})]\ \ \mathrm{d}x + \int_0^{L_i} G' A_3 N_6^T N_6\ \ \mathrm{d}x, \tag{34}$$

$$\mathbf{K}_{i-2} = \frac{1}{2}\int_0^{L_i}\left(\sum_{k=1}^{5}\rho_k A_k\right)[L^2 - (x_i + x)^2]N_5^T N_5\ \ \mathrm{d}x + r\int_0^{L_i}\left(\sum_{k=1}^{5}\rho_k A_k\right)[L - (x_i + x)]N_5^T N_5\ \ \mathrm{d}x, \tag{35}$$

$$\mathbf{F}_i = \int_0^{L_i}\left\{\sum_{k=1}^{5}[\rho_k A_k \dot{\theta}^2(r + x_i + x)N_k^T] - \sum_{k=1}^{5}[\rho_k A_k \ddot{\theta}^2(r + x_i + x)N_4^T] + f_h N_4^T\right\}\ \ \mathrm{d}x + (F_{h_L-x}u_3 + F_{h_L-y}w)|_{i=N}. \tag{36}$$

The final equation of motion, resulting from a standard FEM assembly procedure, is formed as follows

$$\mathbf{M}\ddot{\mathbf{q}} + 2\dot{\theta}\mathbf{C}\dot{\mathbf{q}} + \mathbf{K}\mathbf{q} = \mathbf{F}, \tag{37}$$

with u_1, u_5, w, and $\frac{\partial w}{\partial x}$ being zero at the base of the beam.

4. Experimental results

4.1. Identification of shear modulus values

The detailed specifications of the designed beam are presented in section 2. Other than those physical specifications, the ER fluid has a complex shear modulus, G^*, that needs to be identified for the system at each electric field level. To do so, a set of experiments are conducted on the prototyped beam. The ER fluid-filled beam is clamped to a standard precision dovetail Z-axis stage (ZDTLS80, Misumi, USA) via a custom-made 3D-printed platform. A laser sensor (OADM 20I6441/A14F, Baumer Electric, USA) is attached to a standard precision dovetail XY-axis stage (XYDTS90, Misumi, USA). The two stages are fixed on a setup plate (Misumi, USA), so that the laser is pointed at the center tip of the flexible fin. The laser sensor output is captured by a dSPACE system (RTI 1104, dSPACE, Germany). A high voltage generator power module (Input voltage: 3 V, output voltage: 7 kV, Sunkee, China) is used to generate the desired electric field. For the experiment, the beam is deflected manually around 1 cm at the tip and then released, so the displacement of the tip is recorded using the laser sensor as the beam oscillates. The experiment is repeated 20 times for each electric field value. The experimental setup is shown in figure 8.

From the recorded signals, the natural frequency and the damping ratio of the beam for the given electric field are extracted, which are subsequently used to identify the corresponding G^*. The damping ratio, ζ, is calculated from the two consecutive peaks of the recorded signal (X_c and X_{c+1}, respectively), as follows:

$$\zeta = \sqrt{\frac{1}{\left(\frac{2\pi}{\ln\left(\frac{X_c}{X_{c+1}}\right)}\right)^2}}. \tag{38}$$

The natural frequency, f_n, is obtained from the time instances of two consecutive peaks (T_c and T_{c+1}, respectively) of the recorded signal, as follows:

$$f_n = \frac{1}{(T_{c+1} - T_c)\sqrt{1 - \zeta^2}}. \tag{39}$$

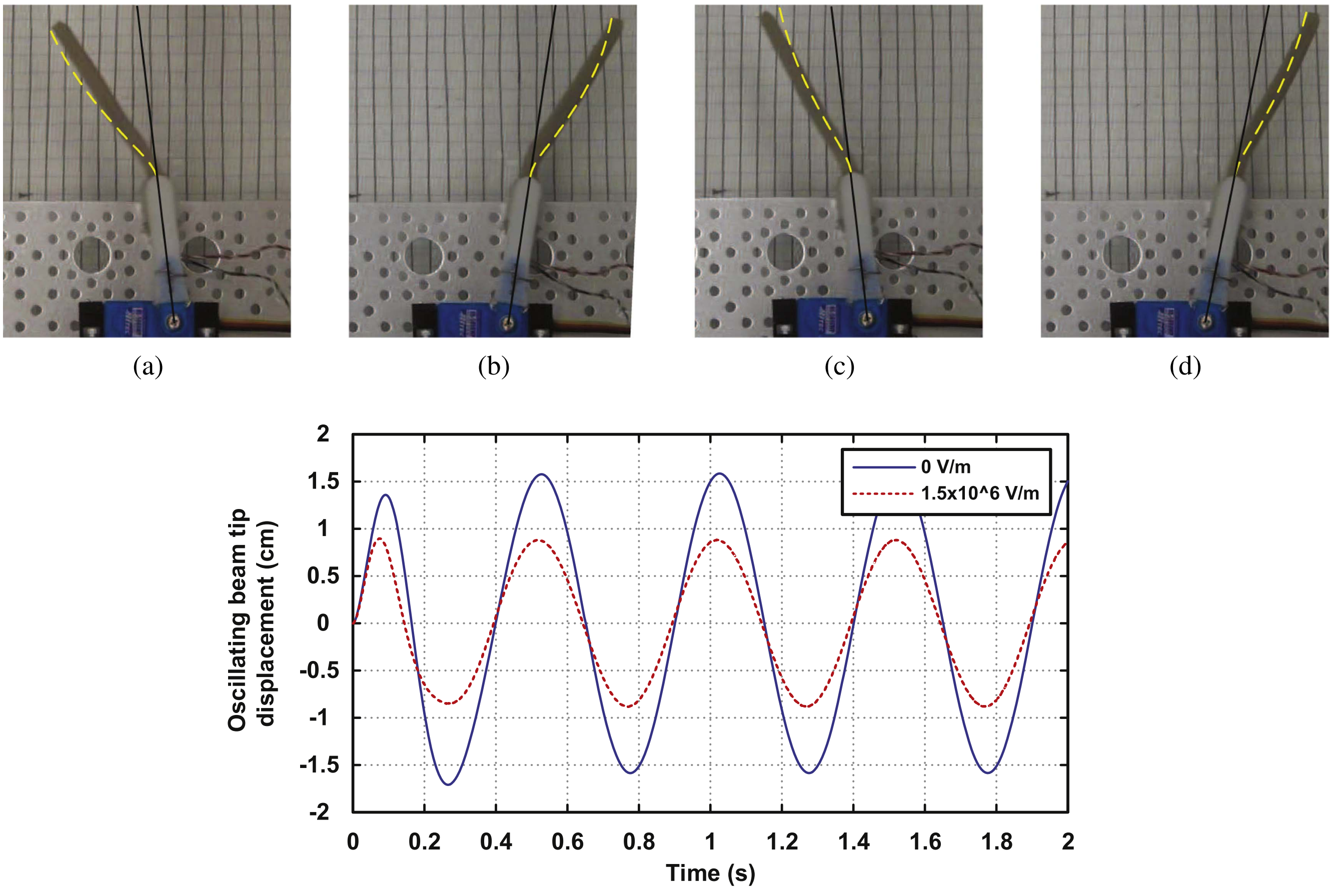

Figure 16. Base-actuated stiffness-tunable fin with fin-beat amplitude of 22.5° and frequency of 2 Hz: (a) and (b) comparison between experimental measurement of the time-dependent beam shapes with model predictions, where the electric field applied to the beam is $E_f = 0$ V m^{-1}, (c) and (d) comparison between experimental measurement of the time-dependent beam shapes with model predictions, where the electric field applied to the beam is $E_f = 1.5 \times 10^6$ V m^{-1}, where the solid black line corresponds to the servo arm direction and the yellow dashed line represents the fin shape by the dynamic model, and (e) comparison between the simulated tip displacements under the two different electric fields.

To identify the parameters G' and G'', we use exhaustive search in range [0, 50000] for G' and [0, 5000] for G'', based on the typical reported values of ER fluids [34, 44]. Specifically, we start with a coarse grid and evaluate the resulting normalized error

$$\epsilon = \left(\frac{f_n^{\mathrm{Sim}} - f_n^{\mathrm{Exp}}}{f_n^{\mathrm{Exp}}}\right)^2 + \left(\frac{\zeta^{\mathrm{Sim}} - \zeta^{\mathrm{Exp}}}{\zeta^{\mathrm{Exp}}}\right)^2. \quad (40)$$

After finding the minimum value for ϵ, we search in a finer grid around the corresponding G' and G''. This procedure is repeated until the error drops bellow 5% for both ζ and f_n. Figures 9(a) and (b) show the empirical damping ratio, ζ, and natural frequency, f_n, for different electric fields, respectively. The damping ratio increases from 0.09 to 0.25 (170% change) and the natural frequency increases from 8.1 to 10.1 Hz (25% change), when the electric field is increased from 0 to 1.5×10^6 V m^{-1}. One can see how increasing the electric field affects the performance of the beam. In the absence of the electric field, the fin is at its most flexible configuration, and thus has the lowest natural frequency. By increasing the electric field, the natural frequency and damping ratio of the flexible fin increase, and it becomes stiffer.

The storage modulus G' and the loss modulus G'' are identified to be

$$G' = 10^3 \times (0.053E_f^3 - 0.043E_f^2 + 0.295E_f + 0.588), \quad (41)$$

$$G'' = 1.33E_f^2 + 33.8E_f + 74.8, \quad (42)$$

where E_f is the electric field applied to the ER fluid. Figure 10 shows the identified complex shear modulus values and the fitted curve under different electric fields. Matlab command `polyfit` is used to fit a third-order polynomial to the identified storage modulus and a second-order polynomial to the identified loss modulus. These parameters are used throughout simulation of all other experimental settings (passive damped oscillations and base-actuated rotations) discussed in the rest of this section. Figure 11 shows both the

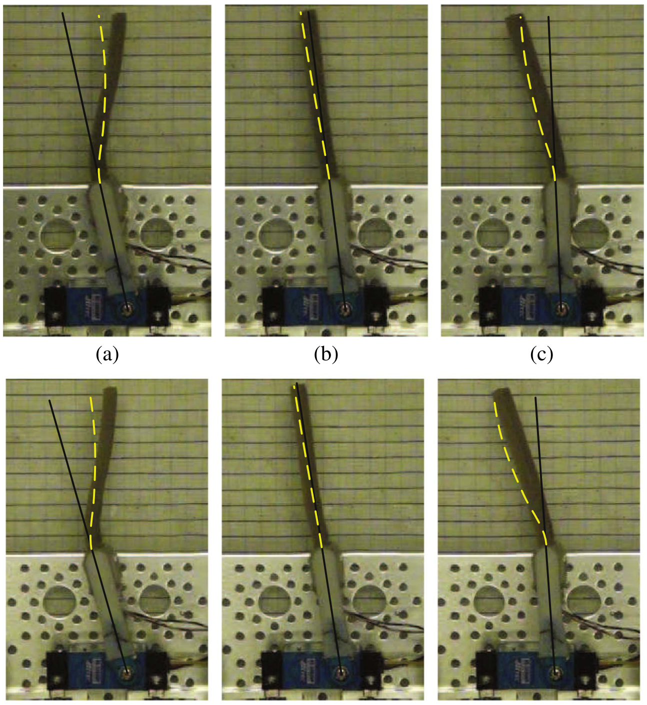

(a) (b) (c)

(d) (e) (f)

Figure 17. Base-actuated stiffness-tunable fin with fin-beat amplitude of 10° and frequency of 4 Hz: (a)–(c) comparison between experimental measurement of the time-dependent beam shapes with model predictions, where the electric field applied to the beam is $E_f = 0$ V m^{-1}, (d)–(f) comparison between experimental measurement of the time-dependent beam shapes with model predictions, where the electric field applied to the beam is $E_f = 1.5 \times 10^6$ V m^{-1}, where the solid black line corresponds to the servo arm direction and the yellow dashed line represents the fin shape by the dynamic model.

simulation and experimental data on the tip displacement of ER fluid-filled flexible fin for different electric field values.

4.2. Identification of hydrodynamic coefficients

A similar set of experiments, but with the proposed stiffness-tuning fin submersed in water, are conducted to identify the complex hydrodynamic coefficient, Γ, in equation (6). The experimental setup is shown in figure 12. The beam is deflected manually around 1 cm at the tip and then released to generate passive, damped oscillations, which are recorded using the laser sensor. The experiment is repeated 20 times for each electric field value. The natural frequency and the damping ratio are extracted from the recorded signal, and are matched to the ones from the simulation to identify the complex hydrodynamic coefficient. Figures 13(a) and (b) show the empirical damping ratio, ζ, and natural frequency, f_n, for different electric fields, respectively, when the beam is in water. The damping ratio increases from 0.18 to 0.42 (130% change) and the natural frequency increases from 3.64 to 5.12 Hz (40% change), when the electric field is increased from 0 to 1.5×10^6 V m^{-1}. Note that the natural frequency and damping ratio decrease when the beam is submersed in water (versus the case when it is in air). The same procedure as described in section 4.1 is applied to find complex hydrodynamic coefficient, $\Gamma = \Gamma' + \mathrm{i}\Gamma''$, with range [0, 10] for both Γ' and Γ''. The identified values of Γ are close to each other for all the tested electric field values; therefore, we consider the mean of the identified values for different electric fields to be the complex hydrodynamic coefficient, which is

$$\Gamma = 4.31 + \mathrm{i}3.84. \tag{43}$$

Note that the complex shear modulus used in these simulations is identified as discussed in section 4.1. Figure 14 shows the comparison of experimentally observed damped oscillations with the simulated ones using the identified hydrodynamic coefficient, where we can see that they match well.

4.3. Base actuation experiments for model validation

The last set of experiments involves actuating the flexible fin in water on its base with a servomotor, emulating the configuration of an anchored robotic fish flapping its tail. The purpose is to examine the stiff-tuning behavior in this new setting and to validate the identified dynamic model with independent experiments. The flexible fin is actuated with a waterproof servo (HS-5086WP from Hitec), fixed in the tank, and the motion of the fin is recorded from above using a high-speed camera (Casio Exilim EX-FH25) at 120 frames s^{-1}. The experimental setup is shown in figure 15.

Figure 16 compares the measured time-dependent beam shapes and those predicted by the dynamic model for fin-beat amplitude of 22.5° and frequency of 2 Hz, for two different electric fields, 0 V m^{-1} (figures 16(a) and (b)) and 1.5×10^6 V m^{-1} (figures 16(c) and (d)). To be brief, we show the first and last frames of each half-cycle. It can be seen that, with an increasing electric field, the fin becomes stiffer and as a result, the tip displacement gets smaller, and good agreement between the experimental and simulation results provides validation of the proposed dynamic model. The comparison of the simulated time-dependent ER fluid filled flexible beam tip displacements for the two electric field values is further shown in figure 16(e).

Finally, we conduct similar experiments with fin-beat frequency of 4 Hz, which is close to the natural frequency of the fin in water. To achieve this flapping frequency, the amplitude of the servo motion is reduced to $\theta_A = 10°$, in order for the servo to stay under its actuation limit. The high-speed camera is set to record at 240 frames s^{-1}. Figure 17 shows the comparison between experimental measurements of the time-dependent fin shapes with model predictions. Overall, the model-predicted beam shape trajectories match well with the model predictions. The discrepancy between the model prediction and the experimental measurement can be attributed to some limitations in the prototyping process. First, the fin was not perfectly symmetric and there was a small difference between liquid urethane rubber thicknesses on the two sides. There was no precise control on the amount of the rubber that leaked on the surface of the copper electrodes during the prototyping procedure, which resulted in another factor in breaking the symmetry. In addition, the bonding agent used to seal the two halves of the beam together was not considered in the modeling procedure. This bonding agent resulted in a stiffer beam than expected. Finally, we note that, due to the measuring range of the laser sensor (30–70 mm), the fin was placed relatively close to the tank wall in the experiments. The effect of the wall on fluid movement around the fin, which was not incorporated in the modeling, could also have contributed to the mismatch between the model prediction and the experimental measurement.

5. Conclusion and future work

The goal of this work was to introduce a novel compact mechanism for a flexible fin with actively tunable stiffness. This was achieved by embedding ER fluid in flexible rubber, and it was demonstrated in experiments that the stiffness could be tuned at a fast speed. A dynamic model derived using Hamilton's principle was proposed to capture the fin's behavior, where the hydrodynamic force on the fin was incorporated. The model parameters were identified with passive oscillation experiments in air and in water, and the model was further validated with base-actuation experiments emulating a flapping fin setting.

The investigation on the stiffness-tunable fins will be extended in several directions. First, the fabrication procedure for the fin will be refined so that the limitations discussed in section 4.3 are addressed. Second, the stiffness-tunable fin will be integrated with a free-swimming robotic fish, to investigate the active onboard control of stiffness when the robot operates in different regimes (fast/slow speeds, for example), for optimization of the swimming efficiency.

Acknowledgments

This work was supported in part by National Science Foundation (Grants IIS-1319602, ECCS 1446793, and CCF-1331852) and a MichiganState University DFI grant.

References

[1] Breder C M and New York Zoological Society 1926 *The Locomotion of Fishes* (*Aquarium Nature Series*) (New York: Office of the Society)
[2] Newman J N and Wu T Y 1975 Hydrodynamical aspects of fish swimming *Swimming Flying Nat.* **2** 615–34
[3] Barrett D S 1996 Propulsive efficiency of a flexible hull underwater vehicle *PhD Dissertation* Massachusetts Institute of Technology
[4] Fan R, Yu J, Wang L, Xie G, Fang Y and Hu Y 2005 Optimized design and implementation of biomimetic robotic dolphin *IEEE Int. Conf. on Robotics and Biomimetics (ROBIO)* pp 484–9
[5] Liu J and Hu H 2010 Biological inspiration: from carangiform fish to multi-joint robotic fish *J. Bionic Eng.* **7** 35–48
[6] Low K 2009 Modelling and parametric study of modular undulating fin rays for fish robots *Mech. Mach. Theory* **44** 615–32
[7] Behbahani S B and Tan X 2016 Design and modeling of flexible passive rowing joints for robotic fish pectoral fins *IEEE Trans. Robot.* **32** 1119–32
[8] Behbahani S B and Tan X 2016 Bio-inspired flexible joints with passive feathering for robotic fish pectoral fins *Bioinsp. Biomim.* **11** 036009
[9] Tangorra J L, Lauder G V, Hunter I W, Mittal R, Madden P G and Bozkurttas M 2010 The effect of fin ray flexural rigidity on the propulsive forces generated by a biorobotic fish pectoral fin *J. Exp. Biol.* **213** 4043–54
[10] Kanso E and Newton P K 2009 Passive locomotion via normal-mode coupling in a submerged spring-mass system *J. Fluid Mech.* **641** 205
[11] Bazaz Behbahani S, Wang J and Tan X 2013 A dynamic model for robotic fish with flexible pectoral fins *IEEE/ASME Int. Conf. on Advanced Intelligent Mechatronics (AIM) (Wollongong, Australia)* pp 1552–7
[12] Wang J, McKinley P K and Tan X 2015 Dynamic modeling of robotic fish with a base-actuated flexible tail *J. Dyn. Syst. Meas. Control* **137** 011004
[13] Ahlborn B, chman S, Stafford R and Harper R 1997 Experimental simulation of the thrust phases of fast-start swimming of fish *J. Exp. Biol.* **200** 2301–12
[14] Daou H E, Salumäe T, Ristolainen A, Toming G, Listak M and Kruusmaa M 2011 A bio-mimetic design and control of a fish-like robot using compliant structures *15th Int. Conf. on Advanced Robotics (ICAR) (Tallinn)* pp 563–8
[15] Low K H and Chong C W 2010 Parametric study of the swimming performance of a fish robot propelled by a flexible caudal fin *Bioinsp. Biomim.* **5** 046002
[16] Yamamoto I, Terada Y, Nagamatu T and Imaizumi Y 1995 Propulsion system with flexible/rigid oscillating fin *IEEE J. Ocean. Eng.* **20** 23–30
[17] Park Y J, Jeong U, Lee J, Kwon S R, Kim H Y and Cho K J 2012 Kinematic condition for maximizing the thrust of a robotic fish using a compliant caudal fin *IEEE Trans. Robot.* **28** 1216–27
[18] Bazaz Behbahani S and Tan X 2014 A flexible passive joint for robotic fish pectoral fins: design, dynamic modeling, and experimental results *IEEE/RSJ Int. Conf. on Intelligent Robots and Systems (IROS) (Chicago, IL, USA)* pp 2832–8
[19] Bazaz Behbahani S and Tan X 2014 Design and dynamic modeling of a flexible feathering joint for robotic fish pectoral fins *ASME Dynamic Systems and Control Conf. (DSCC) (San Antonio, TX, USA)* p V001T05A005
[20] Bazaz Behbahani S and Tan X 2017 Role of pectoral fin flexibility in robotic fish performance *J. Nonlinear Sci.* 1–27
[21] Clark A J, Tan X and McKinley P K 2015 Evolutionary multiobjective design of a flexible caudal fin for robotic fish *Bioinsp. Biomim.* **10** 065006
[22] Kobayashi S, Ozaki T, Nakabayashi M, Morikawa H and Itoh A 2006 Bioinspired aquatic propulsion mechanisms with real-time variable apparent stiffness fins *IEEE Int. Conf. on Robotics and Biomimetics* pp 463–7
[23] Nakabayashi M, Kobayashi R, Kobayashi S and Morikawa H 2009 A novel propulsion mechanism using a fin with a variable-effective-length spring *IEEE Int. Conf. on Robotics and Biomimetics (ROBIO)* pp 1515–21
[24] McHenry M J, Pell C A and Long J H Jr 1995 Mechanical control of swimming speed: stiffness and axial wave form in undulating fish models *J. Exp. Biol.* **198** 2293–305
[25] Long J, Hale M, Mchenry M and Westneat M 1996 Functions of fish skin: flexural stiffness and steady swimming of longnose gar, *Lepisosteus osseus* *J. Exp. Biol.* **199** 2139–51

[26] Lauder G V, Madden P G A, Tangorra J L, Anderson E and Baker T V 2011 Bioinspiration from fish for smart material design and function *Smart Mater. Struct.* **20** 094014
[27] Ziegler M, Hoffmann M, Carbajal J and Pfeifer R 2011 Varying body stiffness for aquatic locomotion *IEEE Int. Conf. on Robotics and Automation (ICRA) (Shanghai, China)* pp 2705–12
[28] Park Y-J, Huh T M, Park D and Cho K-J 2014 Design of a variable-stiffness flapping mechanism for maximizing the thrust of a bio-inspired underwater robot *Bioinsp. Biomim.* **9** 036002
[29] Nakabayashi M, Kobayashi R, Kobayashi S and Morikawa H 2009 Bioinspired propulsion mechanism using a fin with a dynamic variable-effective-length spring *J. Biomech. Sci. Eng.* **4** 82–93
[30] Lindler J E and Wereley N M 1999 Double adjustable shock absorbers using electrorheological fluid *J. Intell. Mater. Syst. Struct.* **10** 652–7
[31] Nakamura T, Saga N and Nakazawa M 2002 Impedance control of a single shaft-type clutch using homogeneous electrorheological fluid *J. Intell. Mater. Syst. Struct.* **13** 465–9
[32] DiTaranto R A 1965 Theory of vibratory bending for elastic and viscoelastic layered finite-length beams *J. Appl. Mech.* **32** 881–6
[33] Yeh Z-F and Shih Y-S 2005 Critical load, dynamic characteristics and parametric instability of electrorheological material-based adaptive beams *Comput. Struct.* **83** 2162–74
[34] Wei K, Meng G, Zhang W and Zhou S 2007 Vibration characteristics of rotating sandwich beams filled with electrorheological fluids *J. Intell. Mater. Syst. Struct.* **18** 1165–73
[35] Lighthill M J 1971 Large-amplitude elongated-body theory of fish locomotion *Proc. R. Soc.* B **179** 125–38
[36] Bazaz Behbahani S and Tan X 2015 Dynamic modeling of robotic fish caudal fin with electrorheological fluid-enabled tunable stiffness *ASME Dynamic Systems and Control Conf. (DSCC)* vol 3 *(Columbus, OH, USA)* p V003T49A006
[37] Sader J E 1998 Frequency response of cantilever beams immersed in viscous fluids with applications to the atomic force microscope *J. Appl. Phys.* **84** 64–76
[38] Chen Z, Shatara S and Tan X 2010 Modeling of biomimetic robotic fish propelled by an ionic polymer metal composite caudal fin *IEEE/ASME Trans. Mechatronics* **15** 448–59
[39] Chung J and Yoo H H 2002 Dynamic analysis of a rotating cantilever beam by using the finite element method *J. Sound Vib.* **249** 147–64
[40] Wei K, Zhang W, Xia P and Liu Y 2012 Nonlinear dynamics of an electrorheological sandwich beam with rotary oscillation *J. Appl. Math.* **2012** 659872
[41] Fung E and Yau D 2004 Vibration characteristics of a rotating flexible arm with ACLD treatment *J. Sound Vib* **269** 165–82
[42] Block H and Kelly J P 1988 Electro-rheology *J. Phys. D: Appl. Phys.* **21** 1661
[43] Weiss K D, Coulter J P and Carlson J D 1993 Material aspects ot electrorheological systems *J. Intell. Mater. Syst. Struct.* **4** 13–34
[44] Yeh J-Y, Chen L-W and Wang C-C 2004 Dynamic stability of a sandwich beam with a constrained layer and electrorheological fluid core *Compos. Struct.* **64** 47–54
[45] Yalcintas M and Coulter J P 1998 Electrorheological material based non-homogeneous adaptive beams *Smart Mater. Struct.* **7** 128